Laser-Induced Ferroelectric Structural Order in an Organic Charge-Transfer Crystal

Eric Collet, *et al.*

Science **300**, 612 (2003);
DOI: 10.1126/science.1082001

Although the cranium does not appear to differ greatly in overall morphology from those currently known from Sterkfontein Member 4, the form of the tympanic plate of the temporal is more closely akin to that of the chimpanzee than to other temporals from Member 4. Of all the new hominid specimens it is the clavicle that displays a unique and ape-like morphology.

Fauna

The Jacovec orange breccia has yielded several near-complete and complete postcranial bones of the long-legged hunting hyaena *Chasmaporthetes* (Fig. 11), as well as *Parapapio*, *Chasmaporthetes*, *Hippotragus*, colobine, felid, canid, bovine, and tortoise. The brown breccia contains *Chasmaporthetes silberbergi*, *Crocuta*, cercopithecid, felid, canid, Herpestinae, Alcelaphini, Antelopini, Bovinae, and tortoise (*24*). No elements within the Jacovec fauna have been identified that serve as independent chronological indicators or that are in conflict with the absolute dates.

References and Notes

1. P. V. Tobias, in *The Cenozoic of Southern Africa*, T. C. Partridge, R. R. Maud, Eds., (Oxford Univ. Press, New York, 2000), pp. 252–276.
2. T. C. Partridge, *Nature* **275**, 282 (1978); T. C. Partridge, in *The Cenozoic of Southern Africa*, T. C. Partridge, R. R. Maud, Eds. (Oxford Univ. Press, New York, 2000), pp. 100–130.
3. K. Kuman, R. J. Clarke, *J. Hum. Evol.* **38**, 827 (2000).
4. R. J. Clarke, *S. Afr. J. Sci.* **94**, 460 (1998).
5. T. C. Partridge, I. B. Watt, *Palaeontol. Afr.* **28**, 35 (1991).
6. R. J. Clarke, *S. Afr. J. Sci.* **98**, 415 (2002).
7. H. P. Schwarcz, R. G. Grün, P. V. Tobias, *J. Hum. Evol.* **26**, 175 (1996).
8. A. Turner, *Palaeontol. Afr.* **34**, 115 (1997).
9. Partridge made the initial age assignment of 3.0 to 3.5 My in (*25*). For a more detailed discussion of the faunal correlations see the comment by J. K. McKee and the reply by P. V. Tobias and R. J. Clarke in (*26*), as well as (*6*).
10. T. C. Partridge, J. Shaw, D. Heslop, R. J. Clarke, *J. Quat. Sci.* **14**, 293 (1999).
11. S. C. Cande, D. V. Kent, *J. Geophys. Res.* **100**, 6093 (1995).
12. L. R. Berger *et al*. (*27*) claim that Member 2 may be as young as 1.07 to 1.95 Ma. We believe this is unsustainable on stratigraphic and faunal as well as on paleomagnetic grounds [see further discussion in (*6*)].
13. M. J. Wilkinson, thesis, University of the Witwatersrand (1973).
14. M. J. Wilkinson, *J. Archaeol. Sci.* **10**, 515 (1983).
15. M. J. Wilkinson, in *Hominid Evolution: Past, Present, and Future*, P. V. Tobias, Ed. (Liss, New York, 1985), pp. 165–170.
16. D. Lal, J. R. Arnold, *Proc. Indian Acad. Sci. Earth Planet. Sci.* **94**, 1 (1985).
17. D. E. Granger, J. W. Kirchner, R. C. Finkel, *Geology* **25**, 107 (1997).
18. D. E. Granger, P. F. Muzikar, *Earth Planet. Sci. Lett.* **188**, 269 (2001).
19. D. E. Granger, D. Fabel, A. N. Palmer, *Geol. Soc. Am. Bull.* **113**, 825 (2001).
20. ^{26}Al and ^{10}Be are produced at a constant ratio, independent of absolute production rates, which vary with altitude, latitude, and geomagnetic field strength. The ^{26}Al/^{10}Be ratio is therefore robust against production rate variations through time.
21. D. Lal, *Earth Planet. Sci. Lett.* **104**, 424 (1991).
22. Examples of erosion rates determined from ^{26}Al and ^{10}Be in sediment include (*28–31*).
23. J. T. Robinson, *Early Hominid Posture and Locomotion* (Univ. of Chicago Press, Chicago, IL, 1972).
24. J. Kibii, thesis, University of the Witwatersrand (2000).
25. R. J. Clarke, P. V. Tobias, *Science* **269**, 521 (1995).
26. Comment by J. K. McKee and reply by P. V. Tobias, R. J. Clarke, *Science* **271**, 1301 (1996).
27. L. R. Berger, R. Lacruz, D. J. de Ruiter *Am. J. Phys. Anthropol.* **119**, 192 (2002).
28. D. E. Granger, J. W. Kirchner, R. Finkel, *J. Geol.* **104**, 249 (1996).
29. E. T. Brown, R. F. Stallard, M. C. Larsen, G. M. Raisbeck, F. Yiou, *Earth Planet. Sci. Lett.* **129**, 193 (1995).
30. C. S. Riebe, J. W. Kirchner, D. E. Granger, R. C. Finkel, *Geology* **28**, 803 (2001).
31. M. Schaller, F. v. Blanckenburg, N. Hovius, P. W. Kubik, *Earth Planet. Sci. Lett.* **188**, 441 (2001).
32. J. R. Middleton, L. Brown, B. Dezfouly-Arjomandy, J. Klein, *Nuclear Instruments and Methods in Physics Research* **B 82**, 399 (1993).
33. Materials and methods are available as supporting material on *Science Online*.
34. There is an additional ambiguity in the meanlife of ^{10}Be that we did not include in Table 2 (*32*). We use an accelerator mass spectrometry (AMS) standard made by the U.S. National Institute of Standards and Technology (NIST) that yields a ^{10}Be meanlife 14% lower than that previously accepted by many researchers, and thus a lower ^{10}Be/^{9}Be ratio. Because other AMS standards are based on a measured activity (*31*), ^{10}Be production rates based on those standards must be lowered by 14%. If we were to use the larger meanlife of 2.18 ± 0.09 Ma, then revised burial dates for our samples would be 4.09 ± 1.08 Ma, 3.57 ± 0.14 Ma, 3.19 ± 0.31 Ma, 3.15 ± 0.25 Ma, 3.43 ± 0.26 Ma, and 0.03 ± 0.07 Ma, in the order in which they appear in Table 2 (analytical uncertainty only).

35. We thank J. Gulley for assistance in cosmogenic nuclide sample preparation and acknowledge support from the NSF (USA); the National Research Foundation (South Africa); the South African Department of Arts, Culture, Science and Technology; the Embassy of France in South Africa; the J. W. Goethe University, Frankfurt; the De Beers Chairman's Fund; the Ford Foundation; the L.S.B. Leakey Foundation; the National Geographic Society; the Palaeoanthropology Scientific Trust Fund; and the Wenner Gren Foundation for Anthropological Research.

Supporting Online Material

www.sciencemag.org/cgi/content/full/300/5619/607/DC1
Materials and Methods
SOM Text

18 December 2002; accepted 17 March 2003

REPORTS

Laser-Induced Ferroelectric Structural Order in an Organic Charge-Transfer Crystal

Eric Collet,[1,2]* Marie-Hélène Lemée-Cailleau,[1] Marylise Buron-Le Cointe,[1] Hervé Cailleau,[1] Michael Wulff,[3] Tadeusz Luty,[4] Shin-Ya Koshihara,[5] Mathias Meyer,[6] Loic Toupet,[1] Philippe Rabiller,[1] Simone Techert[3,7]

We report the direct observation by x-ray diffraction of a photoinduced paraelectric-to-ferroelectric structural phase transition using monochromatic 100-picosecond synchrotron pulses. It occurs in tetrathiafulvalene-*p*-chloranil, a charge-transfer molecular material in which electronic and structural changes are strongly coupled. An optical 300-femtosecond laser pulse switches the material from a neutral to an ionic state on a 500-picosecond time scale and, by virtue of intrinsic cooperativity, generates self-organized long-range structural order. The x-ray data indicate a macroscopic ferroelectric reorganization after the laser irradiation. Refinement of the structures before and after laser irradiation indicates structural changes at the molecular level.

With the development of ultrafast lasers and reliable optics, it is now possible to induce by a light pulse a phase transition and then to change the macroscopic state and the physical properties of a material (*1*, *2*). These phenomena are highly cooperative; that is, the structural relaxation processes of the electronic excited states after the absorption of photons are not independent, as in conventional excitonic or photochemical absorptions, but entail a photoinduced phase transformation toward a new lattice structure and electronic order. This opens the way for a light pulse to induce symmetry breaking from a stable high-temperature phase and so to establish a new self-organized long-range order. Recent developments in time-resolved x-ray diffraction provide an outstanding opportunity for the direct observation, with the appropriate time resolution, of the photoinduced structural changes and symmetry breaking triggered by a pulsed laser irradiation (*3*).

Previous studies in the solid state using a synchrotron source (*4*) have focused on local photochemical or biochemical effects (*5–7*) occurring on the 100-ps time scale. Faster processes on the 100-fs time scale were studied with laser-driven x-ray sources (*8*, *9*), such as disordering phenomena in films (*10*), surface melting (*11*, *12*), and insulating-to-metal transition (*13*). We present a time-resolved x-ray diffraction study in a molecular charge-transfer

(CT) crystal of the photoinduced structural transformation from the neutral phase (stable at high temperature) to the metastable ionic one. We used an optical laser pump and x-ray probe setup installed around a synchrotron source to perform monochromatic data collection in order to solve structural changes with atomic resolution. The 100-ps time resolution is well adapted to the time scale, and we take advantage of the low divergence and brightness of the synchrotron beam. Previous work using pump and probe optical reflectivity spectroscopy (*14*), which can probe the molecular state, has evidenced the electronic change between the neutral stable state and the ionic metastable one. However, the observation of a structural ordering process could not be achieved. Our x-ray data show that a 300-fs laser pulse triggers a three-dimensional structural ferroelectric order, manifested by a symmetry lowering in the diffraction patterns and structural changes at the molecular level deduced from the analysis of more than 800 unique Bragg peaks.

In some materials, molecular multistability between degenerate or quasi-degenerate states involves changes in the molecular identity, such as charge or spin (*1*). Interactions with lattice degrees of freedom, enhanced in low-dimensional multistable systems, cause strong and fast photoinduced cooperative phenomena. Photoswitching between the macroscopic states is exemplified in some charge-transfer insulating molecular materials of mixed-stack architecture that are readily tuned between competing neutral and ionic ground states (*15*). The mixed-stack sequence of alternating donor (D) and acceptor (A) molecules stimulates cooperative electron transfer. Strong structural and electronic coupling gives rise to a chain multistability (*16*, *17*) (Fig. 1) between a regular neutral state, . . .D^0 A^0 D^0 A^0 D^0 A^0 D^0 A^0. . ., and two degenerate and polar dimerized ionic states, . . .(D^+A^-) (D^+A^-) (D^+A^-) (D^+A^-). . . and . . .D^+) (A^-D^+) (A^-D^+) (A^-D^+) (A^-. . . . The phase transition between macroscopic neutral and ionic states, which are both insulating, requires interchain cooperativity (*16*–*18*). We studied the prototype compound tetrathiafulvalene-*p*-chloranil (TTF-CA, $C_6H_4S_4$-$C_6Cl_4O_2$) in which a long-range ferroelectric ordering of the dimers takes place in the ionic low-temperature phase stable below temperature $T_0 \approx 81$ K (*19*). In such materials, photoinduced phenomena are highly cooperative as evidenced by time-resolved optical reflection spectroscopy, giving rise to the ionic-to-neutral phase transformation below T_0 (*14*, *20*, *21*), as well as the neutral-to-ionic one above T_0 (*14*) that is investigated here. The structural relaxation after an optical excitation (Fig. 1) is not localized on one site but entails a drastic structural relaxation involving several molecules, yielding a one-dimensional nanodomain on a ps time scale. When a sufficient number of nanodomains are simultaneously created after a short laser pulse, the interchain cooperativity leads to a switching toward a new macroscopic state; that is, it manifests itself in the formation of three-dimensional domains of the transformed phase, in contrast with conventional homogeneous photoinduced processes. This phase transformation takes place on the 100-ps time scale, whereas the lifetime of the photoinduced metastable state is well below 1 ms. These multiscale photoinduced phenomena are highly nonlinear because the efficiency, which can be as high as a few hundreds of transformed donor-acceptor pairs per photon, is not simply proportional to the total absorbed photon energy (*14*, *21*).

Time-resolved x-ray diffraction experiments on the neutral-to-ionic photoinduced transformation were performed on the beamline ID09B at the European Synchrotron Radiation Facility (ESRF) with the use of the optical-pump and x-ray probe method [(*5*) and citations within]. The single crystal was cooled by a nitrogen stream to 93 K, at which the high-temperature neutral phase is stable. It was pumped by laser pulses of about 300-fs width at 1.55 eV (800 nm), with the polarization parallel to the CT stack. This is an off-resonant excitation because the CT band is centered on 0.65 eV (*22*). A sufficient photon density is needed in order to excite a large part of the crystal, extending over a few penetration depths (estimated in the 10-μm range). Because the recovery of the equilibrium state occurs in much less than 1 ms, the reversible nature of the transformation allows us to probe the sample by recording the diffraction pattern stroboscopically. The pulsed structure of the synchrotron radiation was used to generate x-ray probing pulses in the 16-bunch ESRF mode. A synchronized chopper was used to select the x-ray pulses of 100 ± 10 ps width. The monochromatic x-ray flux on the sample was 3×10^7 photon/s, fully probing the bulk in the transmission geometry of the experiment.

In the first experiment (*23*), the laser beam delivered 1.7×10^{16} photon/cm^2 per pulse to the sample. The diffraction patterns were recorded for different delays between the x-ray and the laser pulses. After laser irradiation, drastic changes were observed in the intensity of some of the Bragg reflections (Fig. 2), with some decreasing and many others increasing, excluding simple laser-heating effects that only lower the intensities via an increase of the Debye-Waller factor. These intensity changes are a direct signature of a strong structural reorganization in the photoinduced state. We stress that this is characteristic of a phase transformation (coherent three-dimensional domains) and not of independent local photoinduced molecular distortions as in photosensitive proteins (*4*), where intensity changes are below 1%. The structural transformation is completed within about 500 ps, in good agreement with previous optical studies (*14*).

In order to determine the photoinduced structural changes, complete data sets were collected in a second experiment (*24*), again at 93 K with a laser excitation density of 2.8×10^{16} photons/cm^2 per pulse and for two time delays: –2 ns (before the excitation) and +1 ns (transformation completed). The data reduction and the reconstruction of the scattered intensity in the reciprocal space were performed with the use of CrysAlis software (*25*). The extracted lattice parameters at –2 ns (neutral monoclinic phase) are in good agreement with those obtained at 90 K at thermal equilibrium (*19*): **a** = 7.2182(2) Å, **b** = 7.586(1) Å, **c** = 14.474(2) Å, and β = 99.140(1)°. At +1 ns, the resolution used did not permit the observation of any significant change in the position of the Bragg reflections and consequently on the lattice parameters that were extracted, but changes in intensities indicate atomic reorganizations inside the unit cell.

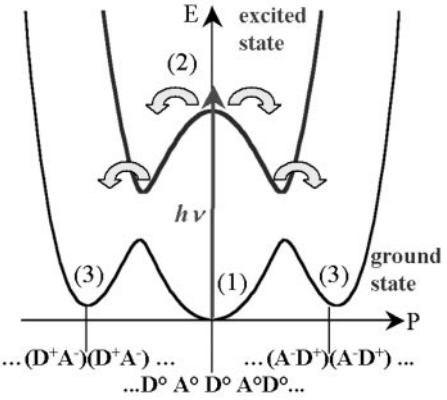

Fig. 1. Schematic drawing of the photoinduced neutral-to-ionic transformation path along the polar order parameter P. The stable neutral state is made of homogeneous, nonpolar neutral chains where electron donor (D) and acceptor (A) molecules are regularly stacked [label (1)]. Photons excite DA pairs into an ionic state [label (2)], and the coupling between the relaxed species makes the system switch to a metastable macroscopic state [label (3)].

[1]Groupe Matière Condensée et Matériaux, UMR CNRS 6626, Université Rennes 1, 35042 Rennes Cedex, France. [2]Laboratoire Léon Brillouin, Commissariat à l'Energie Atomique, Saclay, 91191 Gif-sur-Yvette, France. [3]European Synchrotron Radiation Facility, Boîte Postale 220, 38043 Grenoble, France. [4]Institute of Physical and Theoretical Chemistry, Technical University of Wrocław, 50-370 Wrocław, Poland. [5]Department of Materials Science, Tokyo Institute of Technology, 2-12-1 Oh-okayama, Meguro-ku, Tokyo 152-8551, and Kanagawa Academy of Science and Technology, 3-2-1 Sakado, Takatsu-ku, Kawasaki 213-0012, Japan. [6]Oxford Diffraction Poland Sp. z.o.o., ul. Rogowska 127A, 54-440 Wrocław, Poland. [7]Max Planck Institut for Biophysical Chemistry, Department 010, 37070 Göttingen, Germany.

*To whom correspondence should be addressed. E-mail: Eric.Collet@univ-rennes1.fr

An important feature is the observation from the diffraction patterns of a symmetry lowering in the photoinduced state. Indeed, weak (030) and (0–30) Bragg reflections, absent at –2 ns as forbidden by the symmetry of the neutral phase, clearly appear at +1 ns (Fig. 3). This is the direct signature of the creation of a photoinduced three-dimensional long-range order. It is similar to that occurring in the ferroelectric ionic phase stable at low temperature (*19*), where an important structural reorganization is associated with the change of ionicity. In the high-temperature neutral phase, the monoclinic unit cell contains two symmetry-related undimerized donor-acceptor pairs [space group $P2_1/n$, $Z = 2$ (*26*)]. The molecules regularly stacked along the **a** axis are located on inversion symmetry sites, as schematically shown in Fig. 4. The intrinsic ionicity of the molecules is about 0.3 electron. At $T_0 \approx 81$ K, after a strongly first-order transition, the ionicity increases to about 0.7 electron (*22*). For photoinduced as well as for thermally driven transformations, there is no change in the translational symmetry, but the only appearance in the diffraction pattern of weakly intense (0*k*0) (where $k = 2n + 1$) reflections indicates a symmetry breaking, characterizing the loss of the twofold screw axis (Fig. 4) and, simultaneously, of the inversion center. The space group is then *Pn* ($Z = 2$), implying a ferroelectric long-range order between dimerized ionic chains. The intensity of new (0*k*0) reflections is proportional to the square of the ferroelectric order parameter. For a lower excitation density (0.7×10^{16} photons/cm^2 per pulse), the (030) reflection that is the most intense new one at low Bragg angles was not observed, nor were there significant changes in any other Bragg peak intensities. This result supports the idea that these cooperative photoinduced processes are highly nonlinear. When the number of transformed molecular species is below a critical threshold, the photoswitching cannot take place at the macroscopic scale.

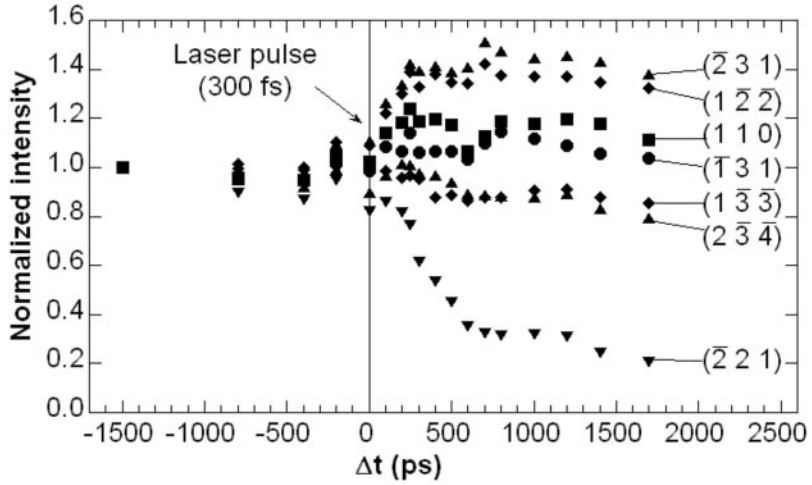

Fig. 2. Relative intensity of some Bragg reflections versus the delay between the laser pump and the x-ray probe. A large structural reorganization, associated with the neutral-to-ionic transformation, follows the laser irradiation. After about 500 ps, the light-driven metastable state is established.

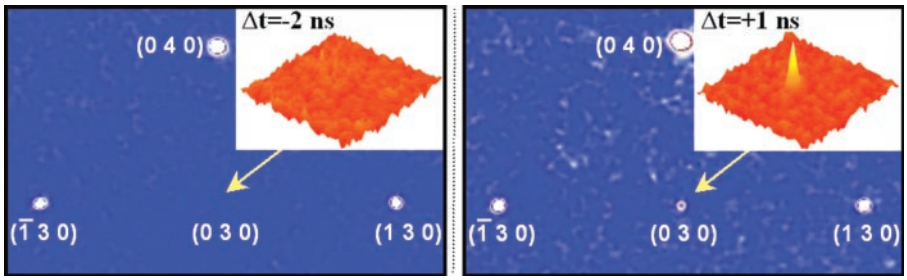

Fig. 3. Reconstructed intensity in the reciprocal (**a***,**b***) planes before ($\Delta t = -2$ ns) and after ($\Delta t = +1$ ns) laser irradiation (largest photon density). The appearance of the (030) reflection, visible directly on the CCD image (inset), signs the ferroelectric nature of the three-dimensional ordered photoinduced state.

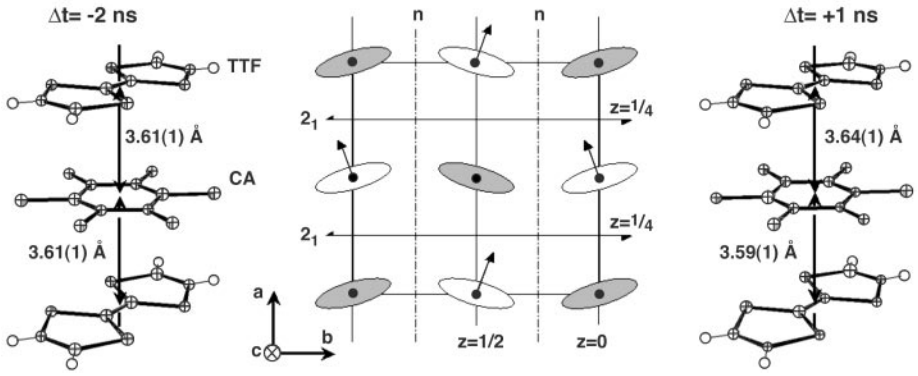

Fig. 4. Schematic drawing (**center**) of the symmetry breaking associated with the phase transition. In the neutral states, TTF (gray ovals) and CA (white ovals) molecules are located on inversion symmetry sites (●), and stacks are related by *n* glide planes and 2_1 screw axes. In the ionic state, the dimerization process represented by arrows occurs mainly along the stacking axis **a**. The simultaneous loss of the inversion center and the screw axis corresponds to a ferroelectric long-range ordering between the stacks. The present study establishes the ferroelectric dimerization distortion between the neutral phase at –2 ns (**left**) and the photoinduced ionic one at +1 ns (**right**).

We refined the structures with the use of the data collection from the high photon density and the SHELX program package (*27*). At –2 ns (*28*), the structure (Fig. 4, left) is in perfect agreement with the neutral structure obtained at thermal equilibrium (*19*), both for the intra- and intermolecular geometries. At +1 ns, because of the symmetry breaking, we refined the structure in the *Pn* space group assuming a full transformation of the crystal. The results obtained from the refinement of many reflections (*28*) indicate a dimerization process in the photoinduced state at +1 ns mainly along the stacking axis **a** (Fig. 4, right) and directly related to the loss of the inversion center of the molecules. This explains the weak intensity of (0 2*n* + 1 0) reflections associated with the symmetry breaking, which are only sensitive to the component of displacements parallel to the **b** axis. The observed structural changes, both for intra- and intermolecular geometries, are again close to the ones observed at thermal equilibrium around the neutral-to-ionic phase transition (*19*). The dimerization amplitude is lower (1/3) than that observed at thermal equilibrium in the ionic ferroelectric phase, and there are two possible reasons for this. First, the amplitude may be intrinsically different in the photoinduced phase. Second, and more likely, the conversion could be incomplete with neutral and transformed ionic ferroelectric phases coexisting. In any case, the results show the macroscopic ferroelectric nature of the photoinduced state.

The above x-ray diffraction signatures evidence the structural reorganization at the photoinduced neutral-to-ionic transformation. The

delay dependence of Bragg reflections intensities shows that the macroscopic transformation is completed in about 500 ps. The most important feature is the evidence of a long-range ferroelectric ordering in the established photo-induced phase. This type of self-organized ordering process driven by light from a high-symmetry phase takes advantage of intrinsic cooperativity, which may also be present in other types of materials. In contrast to optical reflectivity measurements, which are more sensitive to surface, x-ray diffraction probes the bulk. Thus our observations show that the process is highly efficient, in agreement with the weak threshold in excitation intensity at this off-resonant wavelength (*20*). Interesting precursor phenomena, including the seeding process and coherent phonons, have recently been observed by femtosecond reflection spectroscopy under a resonant charge-transfer excitation (*21*). To complement the picosecond investigations, femtosecond x-ray sources will be of fundamental use to study these ultrafast phenomena. Such structural investigations will be essential not only for basic science but also for realizing highly efficient photoswitching devices.

References and Notes

1. K. Nasu, Ed., *Relaxation of Excited States and Photo-induced Structural Phase Transitions* (Springer-Verlag, Berlin, 1997).
2. K. Nasu, H. Ping, H. Mizouchi, *J. Phys. Condens. Matter* **13**, 693 (2001).
3. K. A. Nelson, *Science* **286**, 1310 (1999).
4. M. Wulff, F. Schotte, G. Naylor, D. Bourgeois, *Nucl. Instrum. Methods Phys.* **A398**, 69 (1997).
5. S. Techert, F. Schotte, M. Wulff, *Phys. Rev. Lett.* **86**, 2030 (2001).
6. V. Srajer *et al.*, *Science* **274**, 1726 (1996).
7. G. Busse *et al.*, *Faraday Discuss. Chem. Soc.* **122**, 105 (2002).
8. A. Rousse, C. Rischel, J. C. Gauthier, *Rev. Mod. Phys.* **73**, 17 (2001).
9. A. Cavalleri *et al.*, *Opt. Photonics News* **12**, 29 (2001).
10. C. Rischel *et al.*, *Nature* **390**, 490 (1997).
11. C. W. Siders *et al.*, *Science* **286**, 1340 (1999).
12. A. Rousse *et al.*, *Nature* **410**, 65 (2001).
13. A. Cavalleri *et al.*, *Phys. Rev. Lett.* **87**, 237401 (2001).
14. S. Koshihara, Y. Takahashi, H. Sakai, Y. Tokura, T. Luty, *J. Phys. Chem. B* **103**, 2592 (1999).
15. J. B. Torrance, J. E. Vasquez, J. J. Mayerle, V. Y. Lee, *Phys. Rev. Lett.* **46**, 253 (1981).
16. N. Nagaosa, *J. Phys. Soc. Jpn.* **55**, 3488 (1986).
17. T. Luty *et al.*, *Europhys. Lett.* **59**, 619 (2002).
18. M. H. Lemée-Cailleau *et al.*, *Phys. Rev. Lett.* **79**, 1690 (1997).
19. M. Le Cointe *et al.*, *Phys. Rev. B* **51**, 3374 (1995).
20. K. Tanimura, I. Akimoto, *J. Lumin.* **94–95**, 483 (2001).
21. S. Iwai *et al.*, *Phys. Rev. Lett.* **88**, 057402 (2002).
22. C. S. Jacobsen, J. B. Torrance, *J. Chem. Phys.* **78**, 112 (1983).
23. A single crystal (800 μm by 160 μm by 85 μm) was stroboscopically pumped with a mode-locked Ti:sapphire femtosecond laser (800-nm wavelength), which was synchronized to the x-ray pulses in the storage ring. The polarization of the excitation light was parallel to the stacking axis **a** (the long one), which was also the oscillation axis of the crystal for the x-ray data collections. The synchrotron monochromatic (0.753 Å, Si_{111} monochromator) x-ray probe pulses were selected with a rotating chopper (896 Hz). An exposure time of 2 s was used for oscillations of 2° for different crystal orientations. The diffraction angle 2θ of an image-intensified Princeton charge-coupled device (CCD) camera (camera size was 124 mm by 115 mm, and pixel size was 120 μm by 120 μm) was limited to 30°.
24. Diffraction data were collected with an 850 μm by 140 μm by 140 μm single crystal as in reference (*23*). For each delay, 180 frames were collected, with 4 s and 40 s of exposure and a sample oscillation step of 2° over 360°, on a MAR-CCD camera (size was 133 mm by 133 mm, and pixel size was 64 μm by 64 μm) with 2θ limited to 49°.
25. CrysAlis Software system, Version 1.169, Oxford Diffraction Limited, M. Meyer, Oxford Diffraction Poland (2001).
26. J. J. Mayerle, J. B. Torrance, J. I. Crowley, *Acta Crystallogr.* **B35**, 2988 (1979).
27. G. M. Sheldrick, SHELXL97 program for the refinement of crystal structures and SHELXS97 program for the solution of crystal structures, University of Göttingen, Göttingen, Germany (1997).
28. The quality of the data is characterized by the reliability parameters given in (*27*): $R_{int} = 0.087$ at –2 ns and $R_{int} = 0.066$ at +1 ns. The final refinement at convergence gave $R_1 = 0.054$ and $wR_1 = 0.19$ for 46 parameters with isotropic thermal parameters and a goodness of fit of 1.36 for –2 ns and $R_1 = 0.053$ and $wR_1 = 0.16$ for 91 parameters with isotropic thermal parameters and a goodness of fit of 1.22 for +1 ns. The collected intensities were scaled with more than 6020 observations with $F^2/\sigma(F^2) > 7$, and the average redundancy of 7.2 gave 838 and 1806 unique reflections for –2 and +1 ns, respectively.

29. This work was partly supported by the New Energy and Industrial Technology Development Organization and the Ministry of Education, Science, Culture, and Sports of Japan. E.C. is grateful to the Région Bretagne and CNRS for financial support. S.T. is grateful to the Deutsche Forschungsgemeinschaft for support through the research grant TE 347 / 1-1.

31 December 2002; accepted 10 March 2003

Micellar Nanocontainers Distribute to Defined Cytoplasmic Organelles

Radoslav Savić,[1] Laibin Luo,[2] Adi Eisenberg,[2] Dusica Maysinger[1]*

Block copolymer micelles are water-soluble biocompatible nanocontainers with great potential for delivering hydrophobic drugs. An understanding of their cellular distribution is essential to achieving selective delivery of drugs at the subcellular level. Triple-labeling confocal microscopy in live cells revealed the localization of micelles in several cytoplasmic organelles, including mitochondria, but not in the nucleus. Moreover, micelles change the cellular distribution of and increase the amount of the agent delivered to the cells. These micelles may thus be worth exploring for their potential to selectively deliver drugs to specified subcellular targets.

Unfavorable solubility, stability, and toxicity all hinder the therapeutic efficacy of many drugs and can prevent the approval of investigational pharmacological agents for clinical use. Drug delivery systems (*1–9*) can help by providing a concentration of drugs in an

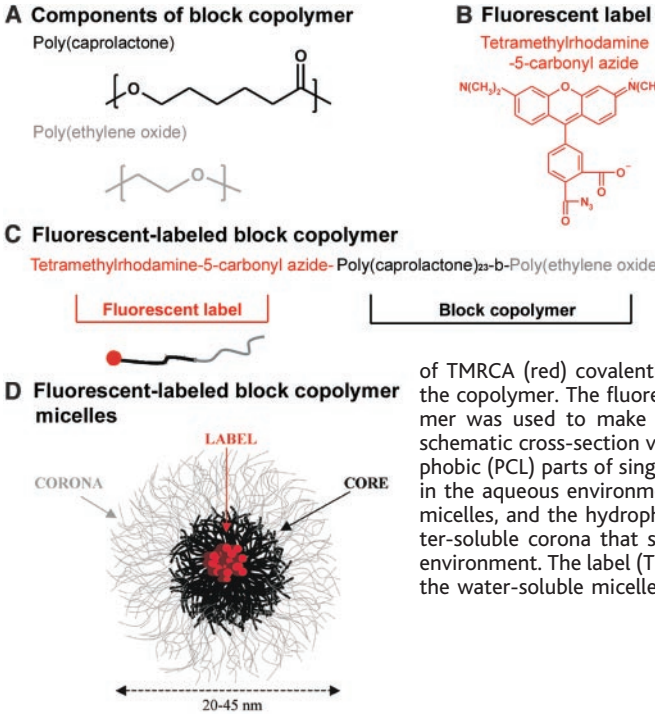

Fig. 1. Schematic drawing of the fluorescent-labeled micelles used. (**A**) The block copolymer was made from PCL and PEO segments. (**B**) The fluorescent label was covalently bound to the PCL part of the block copolymer. (**C**) Each polymer chain consisted of 45 units of PEO (gray) covalently linked to 23 units of PCL (black) and 1 molecule of TMRCA (red) covalently linked to the PCL part of the copolymer. The fluorescent-labeled block copolymer was used to make fluorescent micelles. (**D**) A schematic cross-section view of a micelle. The hydrophobic (PCL) parts of single polymer chains aggregate in the aqueous environment to form the core of the micelles, and the hydrophilic (PEO) parts form a water-soluble corona that separates the core from the environment. The label (TMRCA) resides in the core of the water-soluble micelles.